Reconstructing volcanic plume evolution integrating satellite and ground-based data: Application to the 23rd November 2013 Etna eruption

Matthieu Poret[1, 2], Stefano Corradini[3], Luca Merucci[3], Antonio Costa[1], Daniele Andronico[4], Mario Montopoli[5], Gianfranco Vulpiani[6], Valentin Freret-Lorgeril[7]

[1]Istituto Nazionale di Geofisica e Vulcanologia, Bologna, Italy
[2]University of Bologna, Geophysics department, Bologna, Italy
[3]Istituto Nazionale di Geofisica e Vulcanologia, CNT, Roma, Italy
[4]Istituto Nazionale di Geofisica e Vulcanologia, OsservatorioEtneo, Catania, Italy
[5]Institute of Atmospheric Sciences and Climate, National Research Council of Italy, Roma, Italy
[6]Department of Civil Protection, Presidency of the Councils of Ministers, Roma, Italy
[7] Université Clermont Auvergne, CNRS, IRD, OPGC, Laboratoire Magmas et Volcans, F-63000 Clermont-Ferrand, France

Correspondence to: Matthieu Poret (matthieu.poret@gmail.com)

Abstract. Recent explosive eruptions recorded from different volcanoes worldwide (e.g. Hekla in 2000, Eyjafjallajökull in 2010, Cordón-Caulle in 2011) demonstrated the necessity of a better assessment of the eruption source parameters (e.g. column height, mass eruption rate and especially the Total Grain-Size Distribution – TGSD) to reduce the uncertainties associated with the far-travelling airborne ash mass. To do so, volcanological studies started to integrate observations in order to use more realistic numerical inputs, crucial for taking robust volcanic risk mitigation actions. On 23rd November 2013, Etna volcano (Italy) erupted producing a 10-km height plume, from which two volcanic clouds were observed at two different altitudes from satellite (MSG-SEVIRI, MODIS). One was described as mainly composed by very fine ash (i.e. PM_{20}), whereas the second one as made of ice/SO_2 droplets (i.e. not measurable in terms of ash mass). Atypical north-easterly winds transported the tephra from Etna towards the Puglia region (southern Italy), permitting tephra sampling in proximal (i.e. ~5-25 km from source) and medial areas (i.e. Calabria region, ~160km). Based on the field data analysis, we estimated the TGSD but the paucity of data (especially related to the fine ash fraction) prevented it from being entirely representative of the initial magma fragmentation. To better estimate the TGSD covering the entire grain-size spectrum, we integrated the available field data with X-band weather radar and satellite retrievals. The resulting TGSD is used as input for the FALL3D tephra dispersal numerical model to reconstruct the tephra loading and the far-travelling airborne ash mass. The optimal TGSD is selected by solving an inverse problem through a best-fit with the field, ground-based and satellite-based measurements. The results suggest a total erupted mass of 1.2×10^9 kg, which is very similar to the field-derived value of 1.3×10^9 kg, and a TGSD with a PM_{20} fraction between 3.6 and 9.0 wt%.

Keywords: TGSD; FALL3D; SEVIRI; PM_{20}; tephra dispersal modelling; Eruption Source Parameters

1 Introduction

Volcanic explosive eruptions pose hazards related to the release of large quantity of material into the atmosphere. During such events, the observation of the eruption features such as the eruptive column, the tephra fallout deposit and the far-travelling volcanic plume aims at characterizing the Eruption Source Parameters (ESP). Hazard assessment related to tephra dispersal,

5   and its implications for aviation safety and public health, is one of the major motivations for developing robust automatic tools to forecast airborne ash dispersal and tephra loading (e.g. Macedonio et al., 2005; Costa et al., 2006; Barsotti et al., 2008; Folch et al., 2009). In order to mitigate the risk to aviation traffic, nine VAACs (Volcanic Ash Advisory Centers) were created worldwide for volcanic cloud monitoring purposes. Making use of operational volcanic ash transport and dispersion models, VAACs aim at alerting for the presence of volcanic ash in the atmosphere. Ideally, as input (Folch, 2012), beside other ESPs,

10   such models require the Total Grain-Size Distribution (TGSD), which already has demonstrated to represent one of the most critical ESPs, significantly affecting tephra dispersal model outputs (e.g. Scollo et al., 2008; Beckett et al., 2015). Typically, the TGSD is derived from the field sample analysis through the Voronoi tessellation method (Bonadonna and Houghton, 2005). However, collecting field data on tephra deposit highly depends on the atmospheric conditions, land/sea deposition, site accessibility, etc. As a consequence, when the sample dataset is not adequate in terms of sampling distance from the source

15   (Andronico et al., 2014; Costa et al., 2016a), spatial distribution and density of samples (Bonadonna et al., 2015, Spanu et al., 2016), the field-derived TGSD is uncertain and cannot be assumed as representative of the whole tephra loading and dispersal. Additionally, the atmospheric residence time of the very fine ash (i.e. PM_{20} from hours to weeks; Rose and Durant, 2009) prevents from any rapid deposition implying their substantial under-estimation within the TGSD (Bonadonna et al., 2011; Poret et al., Submitted). This raises the necessity of integrating field data with measurements from other sensors (e.g. ground-

20   based radar and satellite) capable to retrieve the missing information in terms of airborne ash. Recent eruptions (e.g. Hekla in February 2000, Eyjafjallajökull in April 2010, Cordón-Caulle in June 2011) have shown the impact of the very fine ash on air traffic (e.g. Guffanti et al., 2010; Folch et al., 2012) but also on public health (e.g. respiratory diseases; Andronico and Del Carlo 2016; Horwell et al. 2017; Tomašek et al. 2016).

From a computational point of view, the reconstruction of the tephra loading and far-travelling airborne ash dispersal is made

25   by considering a set of ESPs, such as the eruption start and duration, the column height or the Mass Eruption Rate (MER) and the TGSD. This study aims at better constraining the TGSD estimation by integrating field, ground-based and satellite-based measurements. In fact, the non-existence of a single method capable to cover entirely the grain-size spectrum implies such a TGSD should be estimated through an integrated approach. Although, excluding a few studies (Bonadonna et al., 2011; Folch et al., 2012; Poret et al., Submitted), tephra dispersal simulations are commonly run by using the field-based TGSD, here we

30   expanded the reconstruction of the tail of the field-derived TGSD by using radar retrievals and satellite measurements.

Our methodology is applied to the 23rd November 2013 Etna paroxysm, which occurred on the early morning through the New South-East Crater (hereinafter NSEC), being the most active crater in the last 20 years (Behncke et al., 2014; De Beni et al., 2015). Atypical winds dispersed the plume north-easterly driving the tephra towards the Calabria and Puglia regions (~400 km from the source), where ash fallout was reported (Bonaccorso et al., 2014; Andronico et al., 2015; Montopoli, 2016). After the

35   eruption, tephra samples were collected along the plume axis from the volcanic slopes (i.e. 5-25 km from NSEC) to Calabria (i.e. ~160 km; Fig. 1 and Table 1). Meanwhile, the eruption benefited from being observed through ground-based (i.e. X-band weather radar – X-Radar and L-band Doppler radar – VOLDORAD 2B) and satellite-based (i.e. infrared satellite radiometer) remote sensing instruments. Although they operate in different parts of the electromagnetic spectrum, their integration aims at providing a more complete view of the eruption, especially of the plume dynamic.

40   This work aims at producing a constrained TGSD emerging from the integrated approach to reconstruct the tephra loading and the airborne ash dispersal by using the FALL3D tephra dispersal model (Costa et al., 2006; Folch et al., 2009). To assess the TGSD associated with the 23rd November 2013 paroxysm (together with the other ESPs) we first estimated the grain-size distributions derived from i) field and ii) X-Radar data, respectively. Then, we integrated them by weighting the two

distributions to best-fit the measured tephra loadings. Furthermore, we empirically modified the resulting TGSD by enriching the PM_{20} classes until the numerical results reproduce the airborne ash mass retrieved from satellite data. In the scope of assessing the complete initial TGSD, the individual distributions (i.e. field- and radar-derived TGSDs) cannot cover entirely the grain-size spectrum, motivating its achievement by the synergic use of the field, ground-based and satellite retrievals.

5　The paper is organized as follows: Section 2 describes the 23rd November 2013 Etna eruption, the remote sensing and the field measurements. Section 3 reports the TGSD estimation, the modelling approach and methodology used to reproduce the eruption features. Section 4 is devoted to the results together with their discussions. Section 5 presents the main concluding remarks.

2 The 23rd November 2013 lava fountain

10　In 2013, the 17th lava fountain episode took place on 23rd November from the NSEC (De Beni et al., 2015). Mild Strombolian explosions initiated on 22nd November afternoon and increased after 07:00 of the following day (all times are in UTC). The transition between Strombolian and lava fountaining activity (i.e. between resumption and paroxysmal phases; Alparone et al., 2003) started at 09:30, producing lava fountains which increased rapidly in height and intensity. During the 50 min of duration (paroxysmal phase), a sustained 10-km height eruptive column was observed (Bonaccorso et al., 2014; Andronico et al., 2015).

15　Nonetheless, a peculiar feature was recorded (e.g. surveillance cameras from INGV–OE) for this paroxysm by showing a whitish volcanic plume that rose above a brownish one (heavier), from which tephra fallout was visible (Fig. 2). Such observation is attributed to the release of a large amount of water/gas droplets higher than the ejected tephra (Corradini et al., 2016). This is relevant for characterizing the far-travelling airborne ash, which becomes more complex with the presence of two distinct volcanic clouds. Additionally, the presence of volcanic ash in the far-field regions was testified by a A319 pilot

20　who flew over the Albanian coasts at 13:50 at 10.3 km a.s.l. (FL 339), who reported ash between 10.9-11.5 km a.s.l, i.e. FL 360-380 (Crompton and Husson, 2015). The following sub-sections describe the observational data used for this study.

2.1 Field data

Samples were collected and tephra loading per unit area measured at 7 locations (Fig. 1 and Table 1). They were oven-dried at 110 °C for 12 h and analysed in the Sedimentology Laboratory at INGV-OE, in Catania (Italy). The individual Grain-Size

25　Distributions (GSD; available as supplementary material in Fig. S1) were analysed at 1 Φ-interval through the CAMSIZER® (Retsch Technology), covering the range from -5 to 5 Φ (where $d = 2^{-\Phi}$, with the diameter d in mm). Although field measurements are commonly used for determining the Total Erupted Mass (TEM) by integrating the isomass lines (Bonadonna and Costa, 2013), the paucity of samples together with their wide dispersion (Fig. 1) limits the reliability of the estimation based on field observations only. However, on the basis of the field data analysis, Andronico et al. (2015) estimated a TEM of

30　$1.3 \pm 1.1 \times 10^9$ kg making use of the Weibull distribution method (Bonadonna and Costa, 2012). Then, combining the field-derived TEM with the paroxysmal duration (~50 min), they calculated an average MER of $4.5 \pm 3.6 \times 10^5$ kg/s (Andronico et al., 2015). Furthermore, considering the climax phase only (i.e. from 09:55 to 10:14), the MER goes up to 10^6 kg/s ejecting more than 80 wt% of the erupted mass (Donnadieu et al., 2017). It is worth noting that such MER estimations represent average (or peak) value for the entire duration of the paroxysmal phase and do not consider its time evolution. Indeed, in our case the

35　eruption intensity increased and the time-series MER can be assessed from the relationships between MER and the column height (Mastin et al., 2009; Degruyter et al., 2012; Woodhouse et al., 2013; Folch et al., 2016). Hence, to account for the eruptive intensity variation, the calculation would benefit from integration of plume models with measurements of remote sensing systems, which is proposed in this study.

2.2 Satellite and ground based remote sensing data

The eruption was simultaneously observed from both satellites and ground-based instruments. On the first hand, the satellite measurements of plume spreading and airborne ash mass dispersal were collected making use of the Spinning Enhanced Visible and Infrared Imager (SEVIRI) on board the geostationary Meteosat Second Generation (MSG) satellite. The Moderate

5   Resolution Imaging Spectro-radiometer (MODIS) aboard the NASA-Aqua polar-orbit satellite was also used to describe the eruption features (Corradini et al., 2016).

On the second hand, concerning ground-based instruments, the X-Radar (Montopoli 2016, Vulpiani et al., 2016) and the visible/thermal cameras (Corradini et al., 2016) were used to provide time-series data of the plume height and the erupted mass.

10 These observations were integrated to improve the volcanic cloud retrievals, the source characterization and to generate new products based on the multi-disciplinary approach described in Corradini et al. (2016). In particular, the measurements associated with this eruption (Fig. 3) observed the formation of two distinct volcanic clouds moving at their own altitudes towards north-east. Among these two clouds, one appears to reach ~6 km a.s.l. (above sea level) being mainly composed by ash (Ash Cloud – AC) and therefore observable from satellite in terms of airborne ash mass and cloud altitude. The second

15 cloud is higher (~11 km a.s.l.) and made of ice/gas droplets (Ice/gas Cloud – IC) with a dominant characteristic significantly different from the AC blinding the satellite from any ash mass measurement (Prata et al., 2007). As observed at the source, the clouds were united and split out over the Calabria region (around 11:00). As final stage, the AC reached the Puglia region, whereas the IC moved over the Ionian Sea towards Albania (around 14:00). The integration presented in Corradini et al. (2016) permits to reduce the uncertainties associated with the Volcanic Cloud Top Height (VCTH), the volcanic ash/ice/SO_2 Masses

20 (M_a, M_i and M_s in Fig. 4) and the Aerosol Optical Depth (AOD) retrievals. On the basis of the satellite and X-Radar data, Corradini et al. (2016) improved the mass estimation of 30 % and reported a X-Radar-derived TEM of ~3.0×10^9 kg with a PM_{20} fraction between 1-2 wt% in weight. From the onset of the eruption, Fig. 4 shows that ash was dominant until 11:30, from which ice replaced ash. In fact, ash was likely released between 10:00 and 12:00 prior ice (i.e. 11:00-12:45). SO_2 was released all along the eruption (i.e. 10:00-12:30) but the retrievals inferred a lower contribution with respect to the ash and ice.

25 In addition to the VCTH assessment, the source characterization also needs to be better estimated through the ESP together with the eruptive phases. To do so, the plume height time-series is recorded from the visible cameras of the INGV-OE, which indicate values ranging from the NSEC (~3300 m a.s.l.) up to ~11 km a.s.l. with a rapid increase around 9:30 followed by a decay at 10:20.

Besides SEVIRI and X-Radar retrievals, the eruption was also observed through the VOLDORAD 2B radar. In particular, this

30 pulsed Doppler radar operates in the wavelength of 23.5 cm (L-band) allowing lapilli to block-sized to be observed. In fact, VOLDORAD 2B is continuously monitoring Etna's summit craters since 2009 (Donnadieu et al., 2015; Donnadieu et al., 2016) from la Montagnola Station, which is 3 km from the NSEC). Inferred radar parameters (e.g. backscattered echo power) are proportional to the quantity of tephra detected through the radar beam. In addition, the along-beam radial velocities permit lava fountains from being observed at high time resolution (i.e. 0.2 s), inferring near-source ejection velocities by means of

35 the following equation (Freret-Lorgeril et al., 2016):

$$V_e = \frac{v_{r+}}{\sin \theta} \approx 3.89 v_{r+}$$

(1)

where V_e is the ejection velocities (in m/s), v_{r+} is the radial velocity (in m/s) and θ is the elevation angle of the radar beam (here $\theta = 14.9°$). Such approach is relevant for integrating the time-dependant ejection velocities with the corresponding

40 observed eruptive column heights. In particular, we used the VOLDORAD 2B data associated with the 23rd November 2013 eruption to better constrain the eruption phases characterization.

Atmospheric
Chemistry
and Physics
Discussions

3 Methodology

To simulate the tephra loading and airborne ash dispersal related to the 23rd November 2013 Etna eruption, we need to know the related ESPs and in particular the TGSD. Their use aims at describing the eruption column representing the source term through the FPlume model (Folch et al., 2016), which is required by FALL3D tephra dispersal model. In the following
5 methodology, we present the i) TGSD reconstruction used within the ii) modelling approach. Then, the iii) simulations are analysed in terms of tephra loadings and airborne ash mass dispersal to best-fit the field and satellite measurements.

3.1 TGSD estimation

As mentioned above, although the paucity and spatial distribution prevent the 7 field samples from representing fully the whole TGSD (Andronico et al., 2014; Beckett et al., 2015; Bonadonna et al., 2015; Costa et al., 2016a; Spanu et al., 2016), we first
10 estimated the TGSD (hereinafter Field TGSD; Fig. 5) on the basis of the individual GSDs using the Voronoi tessellation method (Bonadonna and Houghton, 2005). However, considering the partial representativeness of the Field TGSD on the erupted material, the information on particle grain-size relative to coarse and fine ash (defined in Rose and Durant, 2009) are retrieved by means of the X-Radar data. In fact, the X-Radar measurements can provide the Particle-Size Distribution (PSD) as ash number density distribution in m^{-3}·mm^{-1} (Corradini et al., 2016). However, the X-Radar-derived PSD also suffers from
15 such partial representativeness of the tephra due to the PSD retrieval uncertainty related to i) the simplifications in the shape of the PSD, which is assumed equal to a gamma distribution model, ii) the Rayleigh particle's scattering regime used to retrieve the PSD parameters and iii) the representability of the model regressions used for parameterizing the PSD parameters as a function of radar measurements.

Then, to retrieve the TGSD from the X-Radar distribution, we converted the PSD into number of particles per unit of volume
20 through the particle-size bins. By means of the volume and density associated with the size bins, we calculated the mass density distribution (hereinafter Radar TGSD; Fig. 5). It is worth noting that these two TGSDs reflect the grain-size distributions observed through the field sampling (i.e. -5 to 5 Φ) or the X-Radar instrument (i.e. -1 to 5 Φ; Corradini et al., 2016), respectively. It follows that assessing accurately the initial TGSD covering both windows can be done by integrating the Field and Radar TGSDs only. Although, in principle, their integration is possible, the different operative grain-size windows prevent
25 them from being merged without knowing their relative weight. This observation explains the substantial difference of the two TGSDs (Fig. 5). Indeed, their integration require the relative weights of the two TGSDs, which is determined empirically by considering integrated distributions ranging from full Field TGSD to full Radar TGSD. To do so, we investigated the weights at regular intervals until we best-fit the field measurements maintaining the shape of the Radar TGSD on the proper grain-size interval (hereinafter Integrated TGSD; Fig. 5).
30 However, due to the instrument/method grain-size limit, none of the three TGSD estimations (Field, Radar or Integrated TGSD; Fig. 5) contains a PM$_{20}$ fraction enough to reproduce the far-travelling airborne ash mass detected by satellite. As in Poret et al. (Submitted), we assessed the tail of the Integrated TGSD by modifying empirically the PM$_{20}$ fraction and adding mass into the corresponding classes (i.e. Φ ≥ 6) through the following parameterization:

$$X(\Phi_i) = X(\Phi_5) \times \gamma^{(\Phi_i - \Phi_5)}$$

35
(2)

where $X(\Phi_i)$ is the fraction (in wt%) allocated to the ith bin, $X(\Phi_5)$ is the fraction obtained for Φ = 5 and γ is the empirical factor ($\gamma < 1$). The explored PM$_{20}$ fractions range between ~0.6-10.7 wt% of the TEM and the optimal fraction to use within the TGSD (hereinafter Whole TGSD; Fig. 5) is chosen on the basis of the reproducibility of both the field and satellite measurements.

3.2 Modelling approach

As input, FALL3D requires an estimation of the ESPs characterising the source (e.g. Costa et al., 2016b). For this aim, we coupled FALL3D with the integral plume model (FPlume; Folch et al., 2016), which describes the eruptive column on the basis of the buoyant plume theory (Morton et al., 1956). In particular, FPlume solves a set of 1D cross-section-averaged

5   equations describing mass, momentum, and energy conservation in the eruption column accounting for wind coupling, air moisture, particle re-entrainment and ash aggregation effects (Folch et al., 2016). To describe the mass flow rate for each particle bin and the distribution within the column, FPlume needs the TGSD with the initial magma temperature and water content. In our case, Etna's magmas have a temperature of 1300 K with ~2.5 wt% (Carbone et al., 2015; Spilliaert et al., 2006). FPlume can calculate the MER from the column height (or vice versa) for a given wind profile (Folch et al., 2016) by describing

10   the air mixing within the plume through two turbulent air entrainment coefficients (i.e. radial – α and cross-flow – β; Bursik, 2001; Kaminski et al., 2005; Suzuki and Koyaguchi, 2015; Folch et al., 2016; Costa et al., 2016b; Macedonio et al, 2016). In our study, α and β are obtained empirically through the solution of an inverse problem (Poret et al., 2017). Ash aggregation is expected to be negligible during Etna eruptions with less than 2 wt% with respect to the fine particles (Poret et al., Submitted). For this reason, we did not consider such process in this study.

15   Tephra dispersal is simulated making use of FALL3D, which is a 3D time-dependent Eulerian model based on the advection-diffusion-sedimentation equation computed over a terrain-following domain (Costa et al., 2006; Folch et al., 2009). Besides the ESPs, FALL3D needs the time-dependent meteorological fields over the computational domain for the corresponding period (i.e. from 00:00 on 23rd up to 24:00 on 28th November 2013). The first series of simulations aim at constraining the computed tephra loadings against the field measurements through a local meteorological database (ARPAE from INGV-OE).

20   ARPAE provides a high spatial (7 × 7 km) and temporal (15 min) resolution over the domain highlighted in Fig. 1. FALL3D internally interpolate the meteorological data over a grid of 1 × 1 km resolution. The related main atmospheric profiles (e.g. temperature, air moisture and wind speed) over the NSEC are displayed in Fig. 6. The use of such high-resolution aims at better capturing the tephra loadings in the proximal and medial areas (Fig. 1 and Table 1).

In the second series of simulations, our goal was to reproduce the satellite retrievals for which the local domain (ARPAE) is

25   not adequate for extending up to Albania at such spatio-temporal resolution. The meteorological fields for the latter domain were obtained from the European Center for Medium-range Weather Forecasts (ECMWF, ERA-Interim-Reanalysis; hereinafter ERA-Interim). They provide 6-hour interval for 37 pressure levels data at 0.75° horizontal resolution. The internal grid resolution is set at 5 × 5 km, which still consistent with the satellite data resolution (3 × 3 km at nadir). For checking the consistency between the two databases, we added the profiles retrieved over NSEC from ERA-Interim in Fig. 6. Although

30   both ARPAE and ERA-Interim tend to have the same temperature and wind speed patterns, the air moisture from ERA-Interim is slightly lower than ARPAE for 3-6 km a.s.l. and higher for 7-11 km a.s.l.. Nonetheless, these observations are not significant to produce a substantial effect on the simulations. In addition to the meteorological database comparison over the NSEC, Fig. 6 shows also the conditions over the Albanian capital (Tirana). Based on the pilot report mentioning ash, the time necessary for the tephra to be transported over Albania is estimated to be of 4:30 h explaining such discrepancy on Fig. 6. Regardless the

35   database, the wind speed indicates moderate to strong wind conditions with higher velocities near the volcano in contrast to Tirana city. As indicative values for 9 km a.s.l., we report ~48 and ~45 m/s over the NSEC (at 09:30) for ERA-Interim and ARPAE, respectively, and ~34 m/s over Tirana city at 14:00. In addition to the velocities, the wind direction (Fig. 6) shows a strong north-easterly orientation over the NSEC, which is consistent with the tephra dispersion towards Calabria. Moreover, the profiles indicate a visible variation between mid- (5-6 km a.s.l.) and high-altitudes (> 7 km a.s.l.), which probably resulted

40   on the different spreading orientations for the two volcanic clouds at their own altitudes as described in Fig. 3. Over Albania, the wind orientation shows a wider span, which explains the spreading of the ice/gas cloud observed by satellite (Fig. 17 in Corradini et al., 2016).

Although tephra dispersal simulations are commonly carried out using the field-based TGSD and assuming a constant average column height (or MER) for the entire duration of the paroxysmal phase (panel a in Fig. 7), it is evident that eruption intensity varies substantially with time and consequently the column height (e.g. Scollo et al., 2014; 2015). To account for such variability, we discretized the eruption into a set of phases in consistency with i) the plume height observations from the remote

5 sensing measurements (Corradini et al., 2016) and ii) the exit velocities calculated through the L-band Doppler radar (VOLDORAD-2B; Donnadieu et al., 2015; 2016; 2017). The improved simulation procedure (panels b and c in Fig. 7) is achieved by coupling this discretization with the Integrated TGSD or the Whole TGSD for the ARPAE or the ERA-Interim databases, respectively.

3.3 Inversion modelling strategy

10 Simulation optimization is carried out by varying the input parameters at constant steps within their ranges facing to the inherent non-uniqueness solution for assessment purposes (e.g. Anderson and Segall, 2013). In our case, we started by inverting the Integrated TGSD made of the weighted Field and Radar distributions. To solve the inverse problem presented above, we simulated the tephra loading using a TGSD given by a weighted average of the Field and Radar TGSDs, ranging from 100 wt% Field TGSD to 100 wt% Radar TGSD with a step of 5 wt% until we best-fit the field measurements.

15 The goodness of the fits was evaluated through different statistical metrics (see Poret et al., 2017). In particular, we used the normalized Root Mean Square Error (i.e. $RMSE$) assuming different error distributions for the tephra loadings and the Aida (1978)'s indexes K (i.e. geometric average of the distribution) and k (i.e. geometric standard deviation of the distribution). The reliability of the simulations is obtained for K between 0.95 and 1.05, which means a threshold of ±5 wt% from the theoretical optimal TEM estimated on the basis of the tephra loading samples. It follows that the best simulations are selected for K close

20 to 1 with k and $RMSEs$ at their minimum. Additionally, we estimated the bias, the correlation and the Student T test (Folch et al., 2010; Gouhier et al., Submitted).

Throughout the simulations, we used the eruption discretization (Sect. 3.2), implying a constant set of column height values, and hence, the corresponding MERs by means of the relationship (Folch et al., 2016). Each phase is achieved with the average exit velocity measured by VOLDORAD 2B. To overcome the non-uniqueness ESP combination, we worked on capturing the

25 sampled tephra loadings by calibrating both the radial and cross-flow entrainment coefficients (α and β) from 0.05 to 0.15 and 0.05 to 1.0, respectively (Costa et al., 2016b).

To account for the satellite retrievals, we used the Whole TGSD exploring a large range of PM_{20} fractions (i.e. from 0.6 to 10.7 wt%; Sect. 3.1) in order to best reproduce the airborne ash dispersal. The optimal fraction is obtained through a quantitative comparison by means of three statistical metrics. As first, we evaluated the difference in terms of mass (i.e.

30 $\Delta Mass$) between the satellite measurements and the FALL3D estimates. To do so, we compared the masses over the number of pixels given by the plume mask (obtained for the threshold of 0.1 t/km^2) retrieved from SEVIRI:

$$\Delta Mass = \frac{1}{\Delta T} \int_{t_0}^{t_f} (M_{Obs} - M_{Sim}) \, dt$$

(3)

where M_{Obs} and M_{Sim} are the observed and simulated masses integrated over the whole event (i.e. from $t_0 = 09:30$ to $t_f =$

35 $14:30$, with $\Delta T = t_f - t_0$). This index gives the discrepancy (in tons) for each γ factor (i.e. PM_{20} fractions). Additionally, we also calculated for each γ factor the absolute average difference of mass per unit area ($\overline{Sum(\Delta)}$ in t/km^2) for the entire volcanic cloud by the following:

$$\overline{Sum(\Delta)} = \frac{1}{\Delta T} \int_{t_0}^{t_f} \frac{\sum_N |M_{Obs}(N) - M_{Sim}(N)|}{Area_P} \, dt$$

Atmospheric
Chemistry
and Physics
Discussions

$$\tag{4}$$

where N is the number of pixels (i.e. plume mask), $M_{Obs}(N)$ and $M_{Sim}(N)$ are the observed and modelled masses associated with the Nth pixel for SEVIRI and FALL3D, respectively. $Area_P$ refers to the area covered for the related time interval, which is calculated by means of N and the pixel resolution (i.e. 9 km^2). This index aims at indicating the uncertainty of the simulated

5   airborne ash mass per unit area with respect to the satellite retrieved

Considering that $\Delta Mass$ and $\overline{Sum(\Delta)}$ are discrepancy estimates, the selection is done on the basis of their minimization. Nonetheless, $\overline{Sum(\Delta)}$ gives absolute values preventing from any over- or under-estimation characterization. It follows that we evaluated also the following index:

$$\varepsilon = \frac{1}{\Delta T} \int_{t_0}^{t_f} \frac{[\sum_N M_{Obs}(N) - M_{Sim}(N) < 0] + [\sum_N M_{Obs}(N) - M_{Sim}(N) > 0]}{Area_P} dt$$

10
$$\tag{5}$$

where ε refers to an over-estimation per pixel when $\varepsilon < 0$ and an under-estimation per pixel for $\varepsilon > 0$, with a best-fit for $\varepsilon = 0$. Moreover, the index indicates the average mass difference per unit area (i.e. t/km^2) between the satellite measurements and the simulation. The synergic use of these metrics aims at providing a robust way of comparing spatially and temporally the simulation outputs and the measurements.

4 Results and Discussion

15

This section first describes the results obtained in terms of best weights to use to obtain the Integrated TGSD reproducing the tephra loadings. Then, we report the results for assessing the PM$_{20}$ fraction needed within the Whole TGSD to reproduce both the tephra loadings and the airborne ash transported in the far field. Beside the ESPs associated with the different TGSDs, we present the simulation results against field, ground-based and satellite measurements.

4.1 ESP inversion

20

The inversion procedure initiated by estimating the Integrated TGSD (Sect. 3.3) through the investigation of weighting factors for both the Field and Radar TGSDs. The corresponding statistical analysis (Table 2) shows the minimum values for $RMSEs$ and k through a large range of combinations. Meanwhile, considering that the $RMSE_1$ and $RMSE_3$ have flat patterns through the weights, we relied on the $RMSE_2$ and k. They show selectable combinations from (65,35; i.e. 65 and 35 in wt% for the

25   Field and Radar TGSDs respectively) to (85,15). Although $RMSE_2$ ranges between 1.56 to 1.85 from (65,35) to (85,15), k is minimized at 2.95 for (75,25) motivating to select this combination as best to compose the Integrated TGSD (Table 2 and Fig. 8). It is worth noting that $RMSE_2$ and k indicate relatively high values yielding a mean error factor nearby 3, which is comparable to uncertainties associated with other classical methods (Bonadonna and Costa, 2012; 2013; Bonadonna et al., 2015).

30   To capture the main airborne ash dispersal feature retrieved from SEVIRI (displayed as animation A1 in the supplementary material), we carried out a quantitative comparison (Sect. 3.3) for different PM$_{20}$ fractions (i.e. 0.6-10.7 wt%). The statistical analysis aims at selecting the correct amount of PM$_{20}$ necessary to ensure the simulation of the ash dispersal. Figure 9 illustrates the inversion by showing the optimization of the statistical indexes. Considering the whole airborne ash mass, the results yield a best value for $\Delta Mass$ at $\gamma = 0.65$ (i.e. PM$_{20} = 9.0$ wt%), indicating an overall under-estimation of 76 tons of ash by FALL3D

35   for the entire eruption. Then, $\overline{Sum(\Delta)}$ shows a minima for $\gamma = 0.40$ (i.e. PM$_{20} = 3.6$ wt%), which gives an absolute average difference of mass per unit area of ~0.37 t/km^2 for the whole sequence. The third index returns an optimal value of $\varepsilon = -0.03$ t/km^2 for $\gamma = 0.65$ (i.e. PM$_{20} = 9.0$ wt%), being consistent with $\Delta Mass$. This index reflects that FALL3D slightly over-estimates the average mass per pixel of 0.03 t/km^2. From the integration of the statistical analysis results (Fig. 9), the Whole

8

TGSD required the minimum PM_{20} fraction of 3.6 wt% to best reproduce in absolute the average ash mass per unit area. However, such a fraction is not sufficient for best simulating the whole airborne ash mass released during the eruption and minimizing the over- or under-estimation, which tends to be satisfied with higher PM_{20} fractions (i.e. 9.0 wt%). The corresponding input TGSD is displayed in Fig. 5. In fact, $\Delta Mass$ and ε in Fig. 9 both indicate that FALL3D under-estimates

5   substantially the airborne mass for PM_{20} fractions lower than ~7 wt% and over-estimates above ~10 wt%.

Regarding the computational parameterization, the column height values were set accordingly to the direct monitoring and X-Radar observations. Considering the high time-dependent variability of the column height (Fig. 7), the MER inverted through FPlume is reported here for the climax phase with $~7.0 \times 10^5$ kg/s. The calibration of the air entrainment coefficients (α and β) returns values ranging from 0.06 to 0.15 and from 0.21 to 1.00 for α and β, respectively, being consistent with the literature

10   (Devenish et al., 2010; Suzuki and Koyaguchi, 2015).

4.2 Tephra loading

During the inversion of the Integrated TGSD, the 6 proximal samples were relatively stable when varying the weight combinations, whereas the farthest measurement (i.e. TER) was substantially affected. Figure 8 shows the comparison between the field tephra loadings and the computed values making use of the Integrated TGSD. It is worth noting that making use of

15   the Field TGSD prevents FALL3D from capturing the TER tephra loading, while the Radar TGSD fails on most of the samples as indicated by the computed values in Table 1. These observations argue the necessity to combine the two different distributions through the Integrated TGSD, especially when field measurements are few. Among the 7 samples, all the proximal ones lie within the 1/5- 5-times the measured tephra loading. The unique medial sample (i.e. TER) is accurately computed with respect to the measurement (all tephra loadings detail is reported in Table 1). Although the 6 proximal field measurements

20   (Table 1) indicate tephra loadings per unit area ranging from 1 to 17 kg/m^2, FALL3D computed them between 3 and 7 kg/m^2 for the Integrated TGSD. Such a lower span compared to the field samples is attributed to the higher difficulty for the model to simulate the very proximal area. Additionally, the location of the field samples with respect to the main plume axis also affects the resulting tephra loadings, especially at such proximal distance (less than 20 km from source).

The numerical results in terms of GSD related to the sampled sites obtained with the Integrated TGSD are compared with the

25   field-derived ones (see Fig. S1 in the supplementary material). In fact, making use of the Integrated TGSD allows FALL3D to reproduce accurately 3 of the 7 samples by peaking at the same modes. However, 4 proximal samples (i.e. CRT, PDM, FFD and GDN) have the mode shifted by 1 Φ, which indicates that the field measurements are slightly finer than the computed ones. As described above, the discrepancy is related to the difficulty for computing accurately at such proximal areas. Nonetheless, the mode shift can also be attributed to the sampling distance from the source as explained in Spanu et al. (2016).

30   Indeed, at proximal area the coarse material ($-4 \geq \Phi \geq -2$) is depositing rapidly, increasing the difficulty of estimating accurately this part of the TGSD by means of the Voronoi tessellation method together with a paucity of field measurements (Andronico et al., 2014). Moreover, we cannot exclude partial breakages of few coarse-grained clasts when impacting the ground (Andronico et al., 2015), which also may result on grain-sizes slightly finer than expected.

As described in Sect. 3.2, we improved the numerical description of the eruption phases accompanied by the input TGSD

35   estimation, which aims at capturing both the tephra loading and airborne ash dispersal. Nonetheless, we run a simulation through the simplified procedure (panel a in Fig. 7) to highlight the difference in terms of tephra loading with the panel b (Fig. 7). The statistical analysis shows that making use of a constant plume height for the entire paroxysmal phase (here ~11.3 km a.s.l.) gives $K = 1.01$ and $k = 5.76$ with $RMSE_1 = 0.80$, $RMSE_2 = 3.36$ and $RMSE_3 = 1.33$, which are significantly higher than for the improved procedure (panel b in Fig. 7 and Table 2). Regarding the TEM, the simplified scheme returns 1.5×10^9 kg,

40   which is ~34 % higher than for the integrated approach with 1.2×10^9 kg. In contrast, the latter TEM is in agreement with the estimation of 1.3×10^9 kg reported in Andronico et al. (2015). It is worth noting that, varying the weighting factors from 100 wt% Field TGSD towards 100 wt% Radar TGSD, yields an increasing TEM going from 1 to 6×10^9 kg, respectively (Table

2). This observation is consistent with the results described in Corradini et al. (2016), which indicates a total mass of 3.0×10^9 kg retrieved from the radar compared to the field-derived TEM of 1.3×10^9 kg of Andronico et al. (2015). Such a difference between X-Radar and field-based estimates of the TEM can be explained by considering the following aspects: i) X-Radar samples airborne particles during their fallout whereas the field measurements are based on deposited tephra; ii) the operative

5   window focuses the X-Radar retrievals on detecting the ash particles (-1 to 5 Φ), while the field sampling method expands the measurements to block-sized (-5 to 5 Φ); iii) The Radar TGSD refers to the average over the duration observed from the radar at the sampled grid points, which not necessarily coincides with the duration and location characterized by the Field TGSD; iv) as explained in Sect. 3.1, the X-Radar measurements are made by means of some assumptions and using a regression model of radar simulations, which can add a further degree of uncertainty. However, the presented integrated approach by weighting

10 the distributions issued from different methods aims at preventing the resulting Integrated TGSD from being associated with the full uncertainty of a single source.

To study the far-travelling airborne ash, we used the simulation procedure displayed on the panel c in Fig. 7, which refers to the wider computational domain (ERA-Interim). Although the quantitative comparison was carried out by means of other statistical metrics than for the tephra loading validation (Sect. 3.3), the simulations were constrained in terms of tephra loading

15 by converging towards the TEM computed through the Integrated TGSD with the ARPAE database. It results that the tephra loading scale reported on the following maps (Fig. 10) indicates slightly different tephra loadings than the values in Table 1 (ERA-Interim). Indeed, Fig. 10 does not aim at comparing the tephra loading values at the sampled sites but is used in terms of whole tephra dispersal validated by the affected areas (e.g. Calabria and Puglia regions).

Making use of the different TGSDs reported in this study, we produced the associated tephra loading maps in Fig. 10. The

20 figure aims at showing that by means of the Field TGSD (panel a), FALL3D was able to simulate the tephra loadings at the sample sites up to Calabria but not the Puglia region, where ash was reported. The Radar TGSD (panel b) operates in the ash window preventing its use from reproducing any tephra loading and airborne ash. In contrast, the Integrated and Whole TGSDs (panels c and d) both capture the tephra loadings, but only the Whole TGSD succeed on simulating the far-travelling airborne ash mass. The corresponding time-series animation of the tephra loading associated with the Whole TGSD is available as

25 supplementary material (Animation A2).

4.3 Airborne ash dispersal

As mentioned in Sect. 2, during the paroxysmal phase, the eruption released simultaneously large quantities of ash, ice and gas (Fig. 4) preventing the remote systems from observing and quantifying the whole event easily. In our case, the formation of two volcanic clouds (AC and IC) following two different trajectories at their own altitudes (i.e. ~6 km for AC and ~11 km

30 for IC; Fig. 3) increased substantially the complexity of comparing quantitatively the far-travelling airborne ash masses (i.e. SEVIRI and FALL3D). Indeed, the columnar satellite measurements and FALL3D results prevent from isolating the two clouds, which motivated this study to focus on the plume mask retrieved by SEVIRI (Fig. 11). The figure aims at illustrating the quantitative comparison carried out between the observed and computed airborne ash mass at each time interval. Considering the inversion of the PM_{20} fraction reported above (Sect. 4.1), we displayed the airborne ash mass maps related to

35 the optimal range of PM_{20}. Indeed, the left column refers to the minimum PM_{20} fraction (i.e. 3.6 wt%) required to capture accurately the absolute average difference of mass per unit area (i.e. $\overline{Sum(\Delta)}$), whereas the right column corresponds to the fraction (i.e. 9.0 wt%) best reproducing the whole airborne ash mass (i.e. $\Delta Mass$ and ε). As example, each panel in Fig. 11 shows the overlap of the SEVIRI retrievals with the FALL3D outputs for a given time. Although the overlap tends to decrease with time, the results related to $\gamma = 0.65$ (i.e. $PM_{20} = 9.0$ wt%) indicate a better performance than for at $\gamma = 0.40$ (i.e. PM_{20}

40 = 3.6 wt%). The entire time-series animations are available in the supplementary material (animations A3 and A4 for $\gamma = 0.40$ and $\gamma = 0.65$, respectively). The reported PM_{20} fraction range is relatively high with respect to the literature (1-2 wt%; Corradini et al., 2016), which can be attributed to the observational data used and the instrument properties. In fact, Corradini

et al. (2016) integrated X-Radar data with satellite retrievals to assess the PM_{20} fraction. However, the satellite does not allow any quantification of mass from pixels mainly filled by ice or gas (e.g. SO_2). In other words, although the volcanic ice/gas clouds are assumed to be produced from ash nucleus (Corradini et al., 2016), the probable presence of ash within such clouds will be missed from SEVIRI.

5   Figure 11 also indicates the presence of the two volcanic clouds (AC and IC) observed from satellite (Corradini et al., 2016), although in our case they are still connected each other. Although they dispersed simultaneously from the source, the FALL3D simulations yield the presence of volcanic ash following the trajectory of AC below FL 250. In addition, FALL3D also indicates a major contribution of the airborne mass associated with the IC trajectory spreading over FL 250. The numerical results in terms of temporal dispersal are corroborated by the SEVIRI observations and the pilot report, which mentioned

10   volcanic ash and probably gas near Albania at FL 360-380 (Crompton and Husson, 2015).
As a consequence of the comparative study, the results reported above represent partially the whole airborne ash. Indeed, only the AC was investigated quantitatively, whereas the IC was just observed. This raises questions related to volcanic hazards, such as the air traffic safety. In fact, on the basis of the FALL3D results, the IC appears to have a significant amount of erupted material (i.e. PM_{20}, ice and gas). This observation highlights the necessity for quantifying entirely the far-travelling airborne

15   erupted material. In particular, this study inferred from quantitative studies based on the observations in terms of tephra loading and airborne ash mass the interest for integrating retrievals from diverse instruments to assess accurately the initial magma fragmentation (i.e. TGSD of the whole erupted tephra).

5 Conclusions

Recent studies have shown the need for improving the assessment of the eruption source parameters to reduce the uncertainties

20   and present more realistic numerical outputs, which can be used for hazards mitigation. Here, we worked on better estimating the initial magma fragmentation (i.e. Total Grain-Size Distribution – TGSD) by integrating measurements from field samples, ground-based (X-band weather radar) and satellite-based (SEVIRI) systems. We applied the methodology on the 23rd November 2013 Etna paroxysm, which benefited from north-easterly winds that dispersed the tephra over the Calabria towards the Puglia and Albania regions. The available observations in terms of tephra loadings and airborne ash dispersal were used to

25   reconstruct numerically (through the FALL3D model) the eruption features from the source to distal areas. In fact, the field-based TGSD reproduces only the sampled tephra loadings, whereas the Radar TGSD refers to a limited range of ash classes preventing its use within FALL3D as initial TGSD. We produced a weighted Integrated TGSD (i.e. weighted average of field + radar distributions) to best-fit the tephra loadings. The inversion results yield a TGSD made of 75 wt% of the Field TGSD and 25 wt% of the Radar TGSD. However, the Integrated TGSD does not account for the far-travelling airborne ash mass

30   observable from satellite (i.e. PM_{20}). To do so, we empirically modified the Integrated TGSD to implement the SEVIRI retrievals by investigating diverse PM_{20} fractions (i.e. 0.6-10.7 wt%), until we best-fit the measurements. The inverted PM_{20} fraction matching the satellite observations appears to range from 3.6 to 9.0 wt% depending on capturing the whole airborne ash mass or the mass per unit area. Although these results in terms of PM_{20} fraction suggest larger values than that reported by Corradini et al. (2016), they reflect the required fractions we used within the input TGSD for best reproducing the satellite

35   retrievals. In fact, the study highlighted the necessity for improving the integration of data together with the quantification of the tephra loading and the airborne mass (i.e. PM_{20}, ice and gas). The TEM related to the Whole TGSD is estimated at 1.2×10^9 kg. This study illustrated the need for integrating the observations from different instrument to achieve a better estimate of the initial TGSD widely used for modelling purposes such as for air traffic safety. This work aims at being of interest for developing new methods or tools capable to assess the TGSD covering entirely the grain-size spectrum.

Atmospheric
Chemistry
and Physics
Discussions

Supplement

The supplement associated with this manuscript serves for illustrating the results in terms of individual grain-size distributions related to the use of the Integrated TGSD, which is validated on the basis of the tephra samples. Then, the time-series animations aim at highlighting the main eruption features (i.e. whole tephra loading and airborne ash dispersal) associated with

5   the use of different input TGSDs.

Figure S1

Comparison of the 7 individuals field-derived GSD with the computed ones through the FALL3D model. The figure indicates the reproducibility of the local GSD by peaking at the correct mode.

Animation A1

10   The time-series animation refers to the dynamic evolution of the volcanic ash cloud travelling from the source retrieved from SEVIRI (i.e. 09:30-14:30 UTC).

Animation A2

The time-series animation corresponds to the simulation of the tephra loading obtained for the Whole TGSD with the empirical γ factor of 0.65. The animation shows the dynamic expansion of the tephra fallout indicating the affected areas (i.e. 09:30-

15   14:30 UTC).

Animation A3

The time-series animation shows the simulation of the airborne ash dispersal associated with the Whole TGSD produced with $\gamma = 0.40$ (i.e. 09:30-14:30 UTC). This animation indicates the dynamic dispersal associated with the initial injection of 3.6 wt% of PM_{20} into the atmosphere. It indicates the presence of a major lobe going towards Albania, which corresponds to the

20   ice/gas volcanic cloud, whereas the minor lobe (i.e. tail) is spreading towards the Puglia region (southern Italy) and is related to the volcanic ash cloud.

Animation A4

The time-series animation is referring to the simulation of the far-travelling airborne ash dispersal computed with the Whole TGSD for the $\gamma = 0.65$ (i.e. 09:30-14:30 UTC). This animation shows a similar dispersal than for the Animation A3. However,

25   making use of $\gamma = 0.65$ means the initial injection of 9.0 wt% of PM_{20} into the atmosphere, which results on higher ash mass values, especially for the major lobe spreading towards Albania.

Author contribution

M. Poret conceived the idea and defined the project approach together with the A. Costa, S. Corradini and L. Merucci. M. Poret and A. Costa compiled the FALL3D simulations and co-wrote the manuscript. S. Corradini and L. Merucci provided

30   and processed the SEVIRI data. G. Vulpiani and M. Montopoli provided and processed the X-band weather radar data. D. Andronico provided and processed the field data. V. Freret-Lorgeril provided and processed the L-band VOLDORAD 2B data. All the co-authors work on the interpretation of the results and finalization of the manuscript.

Competing interests

The authors declare no conflict of interest.

Atmospheric
Chemistry
and Physics
Discussions

References

1.   Alparone, S., Andronico, D., Lodato, L., and Sgroi, T.: Relationship between tremor and volcanic activity during the
10   Southeast Crater eruption on Mount Etna in early 2000. *J. Geophys. Res.*, 108, B5, 2241. doi:10.1029/2002JB001866, 2003.

2.   Anderson, K., and Segall, P.: Bayesian inversion of data from effusive volcanic eruptions using physics-based models: Application to Mount St. Helens 2004-2008, *J. Geophys. Res. – Solid Earth*, 118, 2017–2037. doi:10.1002/jgrb.50169, 2013.

15   3.   Andronico, D., Scollo, S., Cristaldi, A., and Lo Castro, M.D.: Representivity of incompletely sampled fall deposits in estimating eruption source parameters: a test using the 12–13 January 2011 lava fountain deposit from Mt. Etna volcano, Italy, *Bull. Volcanol.*, 76, 861. doi:10.1007/s00445, 2014.

4.   Andronico, D., Scollo, S., and Cristaldi, A.: Unexpected hazards from tephra fallouts at Mt. Etna: The 23 November 2013 lava fountain, *J. Volcanol. Geotherm. Res.*, 304, 118-125. doi:10.1016/j.jvolgeores.2015.08.007, 2015.

20   5.   Andronico, D., and Del Carlo, P.: PM_{10} measurements in urban settlements after lava fountain episodes at Mt. Etna, Italy: Pilot test to assess volcanic ash hazard on human health, *Nat. Hazards Earth Syst. Sci.*, 16, 29–40, 2016.

6.   Barsotti, S., Neri, A., and Scire, J.: The VOL-CALPUFF model for atmospheric ash dispersal. I. Approach and physical formulation, *J. Geophys. Res.*, 113, B03208. doi:10.1029/2006JB004623, 2008.

7.   Behncke, B., Branca, S., Corsaro, R.A., De Beni, E., Miraglia, L., and Proietti, P.: The 2011–2012 summit activity of
25   Mount Etna: birth, growth and products of the new SE crater, *J. Volcanol. Geotherm. Res.*, 270, 10–21. doi:10.1016/j.jvolgeores.2013.11.02, 2014.

8.   Beckett, F.M., Witham, C.S., Hort, M.C., Stevenson, J.A., Bonadonna, C., and Millington, S.C.: Sensitivity of dispersion model forecasts of volcanic ash clouds to the physical characteristics of the particles, *J. Geophys. Res. – Atmos.*, 120. doi:10.1002/2015JD023609, 2015.

30   9.   Bonadonna, C., and Houghton, B.F.: Total grain-size distribution and volume of tephra-fall deposits, *Bull. Volcanol.*, 67, 441–456. doi:10.1007/s00445-004-0386-2, 2005.

10. Bonadonna, C, Genco, R, Gouhier, M, Pistolesi, M, Cioni, R, Alfano, F, Hoskuldsson, A, and Ripepe, M.: Tephra sedimentation during the 2010 Eyjafjallajokull eruption (Iceland) from deposit, radar, and satellite observations, *J. Geophys. Res. – Solid Earth*. doi:10.1029/2011JB008462, 2011.

35   11. Bonadonna, C., and Costa, A.: Estimating the volume of tephra deposits: a new simple strategy, *Geology*, 40, 415–418. doi.org/10.1130/G32769.1, 2012.

12. Bonadonna, C., and Costa, A.: Plume height, volume, and classification of explosive volcanic eruptions based on the Weibull function, *Bull. Volcanol.*, 75, 742. doi:10.1007/s00445-013-0742-1, 2013.

13. Bonadonna, C., Biass, S., and Costa, A.: Physical characterization of explosive volcanic eruptions based on tephra
40   deposits: Propagation of uncertainties and sensitivities analysis, *J. Volcanol. Geotherm. Res.*, 296, 80–100. doi:10.1016/j.jvolgeores.2015.03.009, 2015.

14. Bonaccorso, A., Calvari, S., Linde, A., and Sacks, S: Eruptive processes leading to the most explosive lava fountain at Etna volcano: The 23 November 2013 episode, *Geophys. Res. Lett.*, 41, 4912–4919, doi:10.1002/2014GL060623, 2014.

15. Bursik, M.: Effect of wind on the rise height of volcanic plumes, *Geophys. Res. Lett.*, 28, 3621–3624. doi:10.1029/2001GL013393, 2001.

16. Carbone, D., Zuccarello, L., Messina, A., Scollo, S., and Rymer, H.: Balancing bulk gas accumulation and gas output before and during lava fountaining episodes at Mt. Etna, Sci. Rep. 5, 18049. doi:10.1038/srep18049, 2015.

17. Corradini, S., Montopoli, M., Guerrieri, L., Ricci, M., Scollo, S., Merucci, L., Marzano, F. S., Pugnaghi, S., Prestifilippo, M., Ventress, L., Grainger, R. G., Carboni, E., Vulpiani, G., and Coltelli, M.: A multi-sensor approach for the volcanic ash cloud retrievals and eruption characterization, *Remote Sensing – Special Issue on Volcano Remote Sensing*, 8(1), 58. doi:10.3390/rs8010058, 2016.

18. Costa, A., Macedonio, G., and Folch, A.: A three-dimensional Eulerian model for transport and deposition of volcanic ashes, *Earth Planet. Sci. Lett.*, 241, 634–647. doi:10.1016/j.epsl.2005.11.019, 2006.

19. Costa, A., Pioli, L., and Bonadonna, C.: Assessing tephra total grain-size distribution: Insights from field data analysis, *Earth and Planetary Sci. Lett.*, 443, 90–107, 2016a.

20. Costa, A., Suzuki, Y.J., Cerminara, M., Devenish, B., Esposti Ongaro, T., Herzog, M., Van Eaton, A., Denby, L.C., Bursik, M., de Michieli Vitturi, M., Engwell, S., Neri, A., Barsotti, S., Folch, A., Macedonio, G., Girault, F., Carazzo, G., Tait, S., Kaminski, E., Mastin, L., Woodhouse, M., Phillips, J.C., Hogg, A.J., Degruyter, W.J., and Bonadonna, C.: Results of the eruption column model inter-comparison study, *J. Volcanol. Geotherm. Res.* doi:10.1016/j.jvolgeores.2016.01.017, 2016b.

21. Crompton, E., and Husson, P.: Volcanic Ash Advisories: how the VAACs use the 'Discernible Ash' definition to draw their lines now and in the future, *7th International Workshop on Volcanic Ash (IWVA/7)*, Anchorage (Alaska), USA, 19–23 October, 2015. https://www.wmo.int/aemp/sites/default/files/P-09_Crompton-Husson.pdf

22. De Beni, E., Behncke, B., Branca, S., Nicolosi, I., Carluccio, R., D'Ajello Caracciolo, F., and Chiappini, M.: The continuing story of Etna's New Southeast Crater (2012-2014): Evolution and volume calculations based on field surveys and aerophotogrammetry, *J. Volcanol. Geotherm. Res.*, 303, 175–186. doi:10.1016/j.jvolgeores.2015.07.021, 2015.

23. Degruyter, W., and Bonadonna, C.: Improving on mass flow rate estimates of volcanic eruptions, *Geophys. Res. Lett.*, 39, L16308. doi:10.1029/2012GL052566, 2012.

24. Devenish, B. J., Rooney, G.G., Webster, H.N., and Thomson, D.J.: The entrainment rate for buoyant plumes in a crossflow, *Boundary-Layer Meteorol*. 134, 411–439, doi: 10.1007/s10546-009-9464-5, 2010.

25. Donnadieu F., Freville P., Rivet S., Hervier C., and Cacault P.: The Volcano Doppler radar data base of Etna (VOLDORAD 2B), Université Clermont Auvergne – CNRS. http://wwwobs.univ-bpclermont.fr/SO/televolc/voldorad/bddtr.php. doi:10.18145/VOLDORAD.ETNA.2009, 2015.

26. Donnadieu F., Freville P., Hervier C., Coltelli M., Scollo S., Prestifilipo M., Valade S., Rivet S., and Cacault P.: Near-source Doppler radar monitoring of tephra plumes at Etna, *J. Volcanol. Geotherm. Res.*, 312:26–39, 2016.

27. Donnadieu, F., Freret-Lorgeril, V., Coltelli, M., Scollo, S., Gouhier, M., Fréville, P., Hervier, C., and Prestifilippo, M.: Lava fountaining paroxysms generating tephra plumes at Mt. Etna: Remote sensing retrievals, *IAVCEI meeting*, Portland, 14-18 August 2017, USA, Poster VO43A-139.

28. Folch, A., Costa, A., and Macedonio, G.: FALL3D: A computational model for transport and deposition of volcanic ash, *Comp. Geosci.*, 35, 1334–1342. doi:10.1016/j.cageo.2008.08.008, 2009.

29. Folch, A., Costa, A., Durant, A., and Macedonio, G.: A model for wet aggregation of ash particles in volcanic plumes and clouds: 2. Model application, *J. Geophys. Res.*, 115, B09202. doi:10.1029/2009JB007176, 2010.

30. Folch, A.: A review of tephra transport and dispersal models: Evolution, current status, and future perspectives, *J. Volcanol. Geotherm. Res.*, 235–236, 96–115. doi: 10.1016/j.volgeores.2012.05.020, 2012.

31. Folch, A., Costa, A., and Basart, S.: Validation of the FALL3D ash dispersion model using observations of the 2010 Eyjafjallajökull volcanic ash clouds, *Atmos. Env.*, 48, 165–183. doi:10.1016/j.atmosenv.2011.06.072, 2012.

32. Folch, A., Costa, A., and Macedonio, G.: FPLUME-1.0: An integral volcanic plume model accounting for ash aggregation, *Geosci. Model Dev.*, 9, 431–450. doi:10.5194/gmd-9-431-2016, 2016.

33. Freret-Lorgeril, V., Donnadieu, F., Coltelli, M., Scollo, S., Fréville, P., Hervier, C., and Prestifilippo, M.: Doppler radar retrievals from lava fountaining paroxysms generating tephra plumes at Mt. Etna, *EGU General Assembly*, Vienna, 23-28 April, Poster,2016.

34. Gouhier, M., Eychenne, J., Azzaoui, N., Guillin, A., Deslandes, M., Poret, M., Costa, A., and Husson, P.: Low efficiency of large volcanic eruptions in transporting fine ash into the atmosphere, *Nature – Geosciences*, submitted.

35. Guffanti, M., Casadevall, T.J., and Budding, K.: Encounters of Aircraft with Volcanic Ash Clouds: A Compilation of Known Incidents, 1953-2009. *U.S. Geological Survey Data Series 545*, ver. 1.0, 12 p., plus 4 appendixes including the compilation database, available only at http://pubs.usgs.gov/ds/545, 2010.

36. Horwell, C.J., Sargent, P., Andronico, D., Lo Castro, M.D., Tomatis, M., Hillman, S.E., Michnowicz, S.A.K., and Fubini, B.: The iron-catalysed surface reactivity and health-pertinent physical characteristics of explosive volcanic ash from Mt. Etna, Italy, *J. Appl. Volcanol.* doi:10.1186/s13617-017-0063-8, 2017.

37. Kaminski, E., Tait, S., and Carazzo, G.: Turbulent entrainment in jets with arbitrary buoyancy, *J. Fluid Mech.*, 526, 361–376. doi:10.1017/S0022112004003209, 2005.

38. Macedonio, G., Costa, A., and Longo, A.: A computer model for volcanic ash fallout and assessment of subsequent hazards, *Comp. Geosci.*, 31, 837–845, 2005.

39. Macedonio, G., Costa, A., and Folch, A.: Uncertainties in volcanic plume modelling: A parametric study using FPlume, *J. Volcanol. Geotherm. Res.*, 326, 92–102. doi:10.1016/j.jvolgeores.2016.03.016, 2016.

40. Mastin, L.G., Guffanti, M., Servranckx, R., Webley, P., Barsotti, S., Dean, K., Durant, A., Ewert, J. W., Neri, A., Rose, W.I., Schneider, D., Siebert, L., Stunder, B., Swanson, G., Tupper, A., Volentik, A., and Waythomas, C.F.: A multidisciplinary effort to assign realistic source parameters to models of volcanic ash-cloud transport and dispersion during eruptions, *J. Volcanol. Geotherm. Res.*, 186, 10-21, 2009.

41. Montopoli, M.: Velocity profiles inside volcanic clouds from three-dimensional scanning microwave dual-polarization Doppler radars, *J. Geophys. Res. – Atmos.*, 121. doi:10.1002/2015JD023464, 2016.

42. Morton, B.R., Taylor, G.I., and Turner, J.S.: Turbulent gravitational convection from maintained and instantaneous source, *Phil. Trans. Royal Society*, London, A 234, 1–23, 1956.

43. Poret, M., Costa, A., Folch, A., and Martì, A.: Modelling tephra dispersal and ash aggregation: The 26th April 1979 eruption, La Soufrière St. Vincent, *J. Volcanol. Geotherm. Res*, 347C, 207–220. doi:10.1016/j.jvolgeores.2017.09.012, 2017.

44. Poret, M., Costa, A., Andronico, D., Scollo, S., Gouhier, M., and Cristaldi, A.: Modelling eruption source parameters by integrating field, ground-based and satellite-based measurements: The case of the 23rd February 2013 Etna paroxysm, *J. Geophys. Res – Solid Earth*, submitted.

45. Prata, A.J., and Kerkmann, J.: Simultaneous retrieval of volcanic ash and SO_2 using MSG-SEVIRI measurements. *Geophys. Res. Lett.* 34, L05813. doi:10.1029/2006GL028691, 2007.

46. Rose, W.I., and Durant, A.J.: Fine ash content of explosive eruptions, *J. Volcanol. Geoth. Res.* doi:10.1016/j.jvolgeores.2009.01.010, 2009.

47. Scollo, S., Folch, A., and Costa, A.: A parametric and comparative study of different tephra fallout models. *J. Volcanol. Geoth. Res.* 176, 199–211. doi: 10.1016/j.jvolgeores.2008.04.002, 2008.

48. Scollo, S., Prestifilippo, M., Pecora, E., Corradini, S., Merucci, L., Spata, G., and Coltelli, M.: Eruption column height estimation of the 2011-2013 Etna lava fountains, *Annals of Geophys.*, 57, 2, S0214. doi:10.4401/ag-6396, 2014.

49. Scollo, S., Boselli, A., Coltelli, M., Leto, G., Pisani, G., Prestifilippo, M., Spinelli, N., and Wang, X.: Volcanic ash concentration during the 12 August 2011 Etna eruption, *Geophys. Res. Lett.*, 42. doi:10.1002/2015GL063027, 2015.

50. Spanu, A., Vitturi, M. dé M., and Barsotti, S.: Reconstructing eruptive source parameters from tephra deposit: a numerical study of medium-sized explosive eruptions at Etna volcano, *Bull. Volcanol.*, 78, 59. doi:10.1007/s00445-016-1051-2, 2016.

51. Spilliaert, N., Allard, P., Metrich, N., and Sobolev, A.V.: Melt inclusion record of the conditions of ascent, degassing, and extrusion of volatile-rich alkali basalt during the powerful 2002 flank eruption of Mount Etna (Italy), *J. Geophys. Res.*, 111, B04203. doi:10.1029/2005JB003934, 2006.

52. Suzuki, Y., and Koyaguchi, T.: Effects of wind on entrainment efficiency in volcanic plumes, *J. Geophys. Res. – Solid Earth*, 61, 6122–6140. doi:10.1002/2015JBO12208, 2015.

53. Tomašek, I., Horwell, C.J., Damby, D.E., Barošová, H., Geers, C., Petri-Fink, A., Rothen-Rutishauser, B., and Clift, M.J.D.: Combined exposure of diesel exhaust particles and respirable Soufrière Hills volcanic ash causes a (pro-) inflammatory response in an in vitro multicellular epithelial tissue barrier model, *Particle and Fibre Toxicology*, 13 (1), 67. doi:10.1186/s12989-016-0178-9, 2016.

54. Vulpiani, G., Ripepe, M., and Valade, S.: Mass discharge rate retrieval combining weather radar and thermal camera observations, *J. Geophys. Res. – Solid Earth*, 121, 5679–5695. doi:10.1002/2016JB013191, 2016.

55. Woodhouse, M.J., Hogg, A.J., Phillips, J.C., and Sparks, R.S.J.: Interaction between volcanic plumes and wind during the 2010 Eyjafjallajökull eruption, Iceland, *J. Geophys. Res. – Solid Earth*, 118, 92–109. doi:10.1029/2012JB009592, 2013.

Tables

Table 1: Field measurements compared with the computed tephra loadings

	Field observations					**Computed loading (kg/m^2)**			
Sample	**Location**	**Longitude**	**Latitude**	**Mode (Φ)**	**Loading (kg/m^2)**	**Field TGSD**	**Radar TGSD**	**Integrated TGSD**	**Whole TGSD**
CTL	Citelli	15.060	37.765	-3	1.7×10^1	7.2×10^0	3.4×10^{-1}	4.1×10^0	2.0×10^0
CRT	Cerrita	15.092	37.774	-2	1.4×10^1	5.2×10^0	3.5×10^{-1}	2.8×10^0	2.0×10^0
PDM	Piedimonte	15.177	37.810	-2	6.1×10^0	1.3×10^1	1.3×10^{-1}	6.6×10^0	1.8×10^0
FFD	Fiumefreddo	15.215	37.799	-1	1.6×10^0	9.6×10^0	2.9×10^{-1}	4.9×10^0	1.5×10^0
CPV	Campovolo	15.228	37.801	-2	9.5×10^{-1}	8.6×10^0	3.2×10^{-1}	4.4×10^0	1.4×10^0
GDN	Giardini	15.250	37.819	-1	4.0×10^0	9.8×10^0	3.8×10^{-1}	5.0×10^0	1.4×10^0
TER	T.Ellera	16.548	38.417	3	1.6×10^{-2}	4.0×10^{-4}	3.5×10^{-1}	1.5×10^{-2}	2.4×10^{-2}

Table 1: Field measurements (locations, loadings and modes) with the computed tephra loadings obtained by mean of the ARPAE database for the explored TGSDs (Fig. 5).

5

Table 2: Statistical analysis and TEM estimations during the inversion of the Integrated TGSD

Integrated TGSD	**Statistical Metric**								**Output**
Combination (in wt%)	**K**	**k**	**RMSE$_1$**	**RMSE$_2$**	**RMSE$_3$**	**Correlation**	**Bias**	**TTest**	**TEM ($\times10^9$ in kg)**
Radar TGSD	6.97	9.82	0.97	7.71	0.87	-0.2	-0.3	0.1	5.73
20 Field | 80 Radar	1.00	4.35	0.84	2.95	0.74	0.8	0.0	1.0	2.84
40 Field | 60 Radar	1.02	3.48	0.81	1.61	0.74	0.8	0.0	1.0	1.66
60 Field | 40 Radar	1.01	3.08	0.78	1.53	0.77	0.9	0.0	1.0	1.28
65 Field | 35 Radar	1.01	3.02	0.77	1.56	0.77	0.9	0.0	1.0	1.22
70 Field | 30 Radar	0.98	2.98	0.77	1.67	0.80	0.9	0.0	1.0	1.21
75 Field | 25 Radar	1.02	2.95	0.76	1.64	0.79	0.9	0.0	1.0	1.13
80 Field | 20 Radar	0.99	2.96	0.75	1.77	0.82	0.9	0.0	1.0	1.13
85 Field | 15 Radar	1.01	3.00	0.75	1.85	0.84	0.9	0.0	1.0	1.10
90 Field | 10 Radar	1.00	3.13	0.74	2.02	0.88	0.9	0.0	1.0	1.12
Field TGSD	0.99	6.56	0.83	3.65	1.44	0.9	0.0	1.0	1.60

Table 2: Statistical metric and TEM results related to the explored weighting factors used for assessing the Integrated TGSD (i.e. Field + Radar data).

Atmospheric
Chemistry
and Physics
Discussions

Figure 1: Tephra sample locations (Sicily and Calabria regions, Italy). a) shows the medial area (up to ~160 km from NSEC) affected by the tephra fallout. b) is a zoom of a) indicating the proximal zone (up to ~25 km from NSEC) and the dispersion of the samples. Details in Table 1.
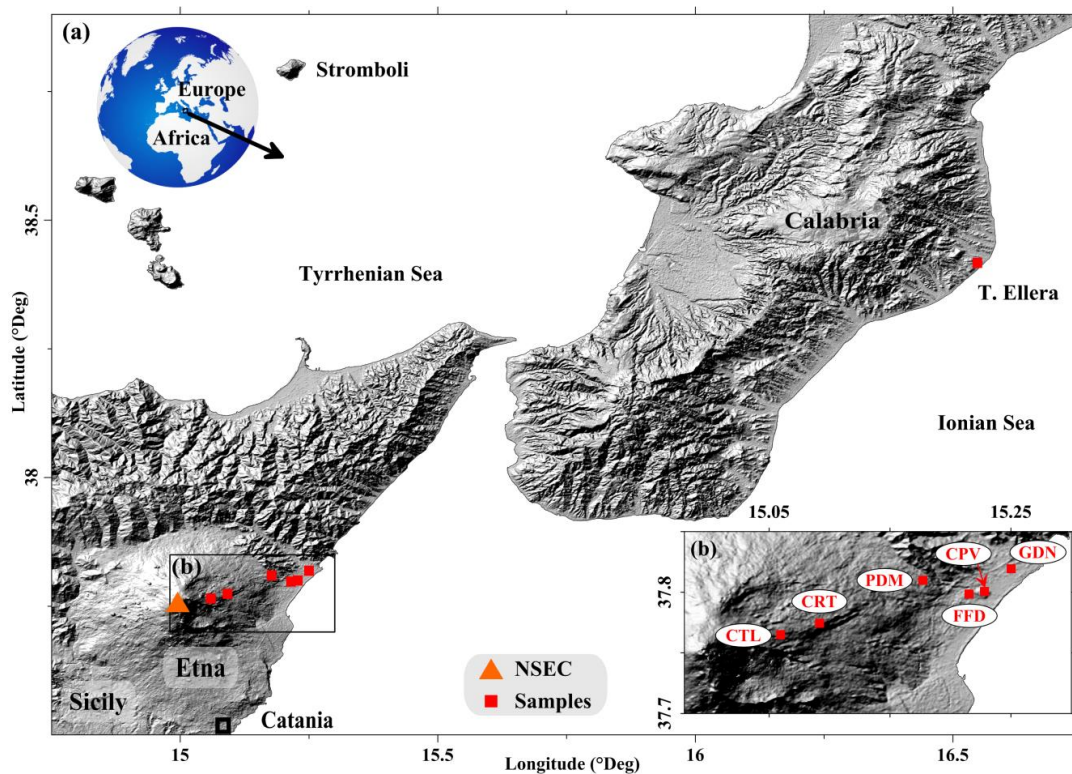
Atmospheric
Chemistry
and Physics
Discussions

Figure 2: Photograph representing the eruption with the two distinct volcanic plumes dispersing at different altitudes (whitish above and brownish below). Source: Courtesy of Boris Behncke (INGV–OE).

Atmospheric
Chemistry
and Physics
Discussions

Figure 3: Satellite image (SEVIRI) showing the trajectories of the two volcanic clouds (modified from Figure 17 in Corradini et al., 2016). The Ash Cloud dispersed towards the Puglia region (southern Italy) at ~6 km a.s.l., whereas the Ice Cloud goes over Albania at ~11 km a.s.l..

Atmospheric
Chemistry
and Physics
Discussions
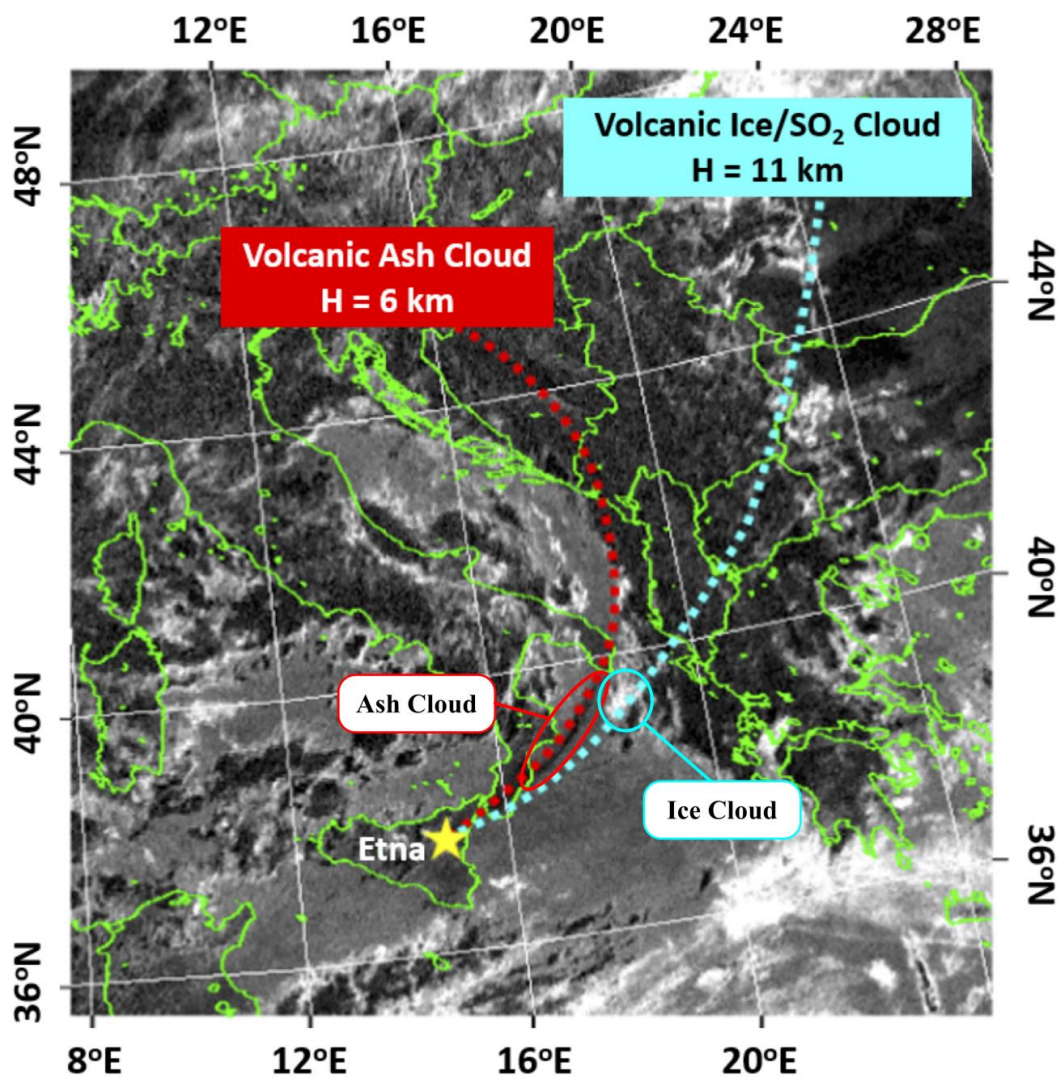
Figure 4: Ash, Ice and SO₂ masses time-series retrieved from SEVIRI during the 23rd November 2013 Etna eruption.
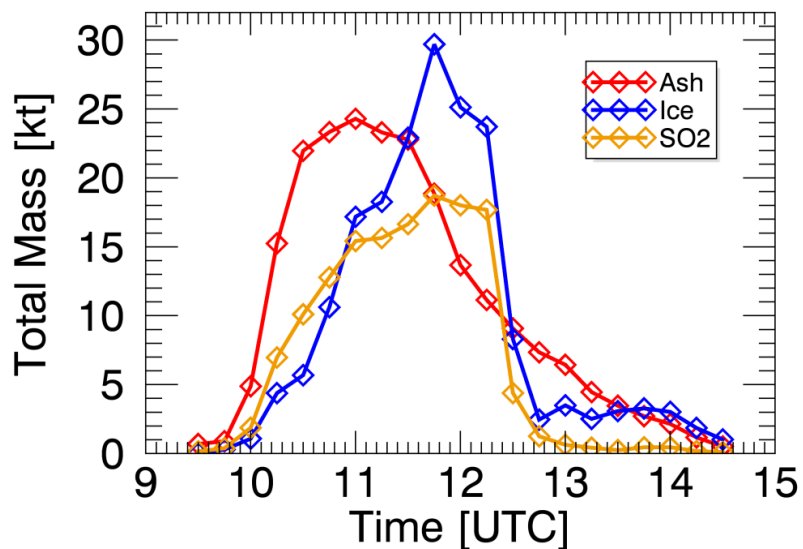
Figure 5: Input TGSDs estimated from either field or X-Radar data. The Integrated TGSD is based on the weighted integration of the Field and Radar TGSDs. The Whole TGSD emerges from the Integrated TGSD implemented with the satellite-based measurements.

Atmospheric
Chemistry
and Physics
Discussions
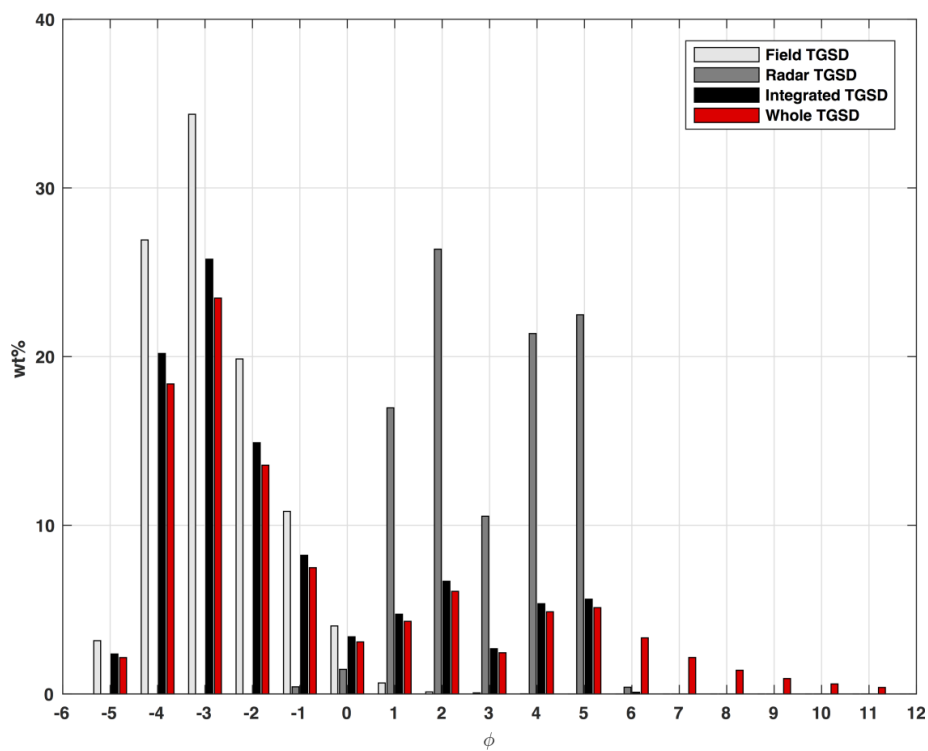
Figure 6: Meteorological fields represented over the NSEC from the ARPAE and the ECMWF (ERA-Interim Reanalysis) platforms and over Tirana city for ERA-Interim.

Atmospheric
Chemistry
and Physics
Discussions
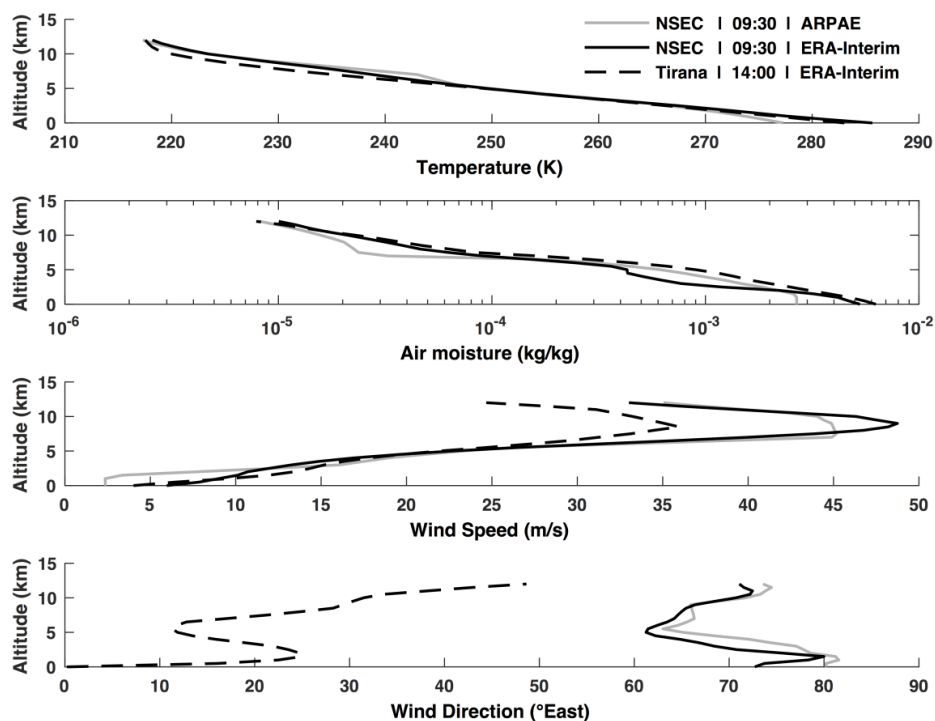
Figure 7: Simulation schemes. a) Simplified procedure. b) Use of the Integrated TGSD (field + X-Radar observations) with the ARPAE meteorological database and the recorded eruptive column heights and exit velocities. c) Use of the Whole TGSD (field + X-Radar + SEVIRI measurements) with ERA-Interim database and the recorded eruptive column heights and exit velocities.
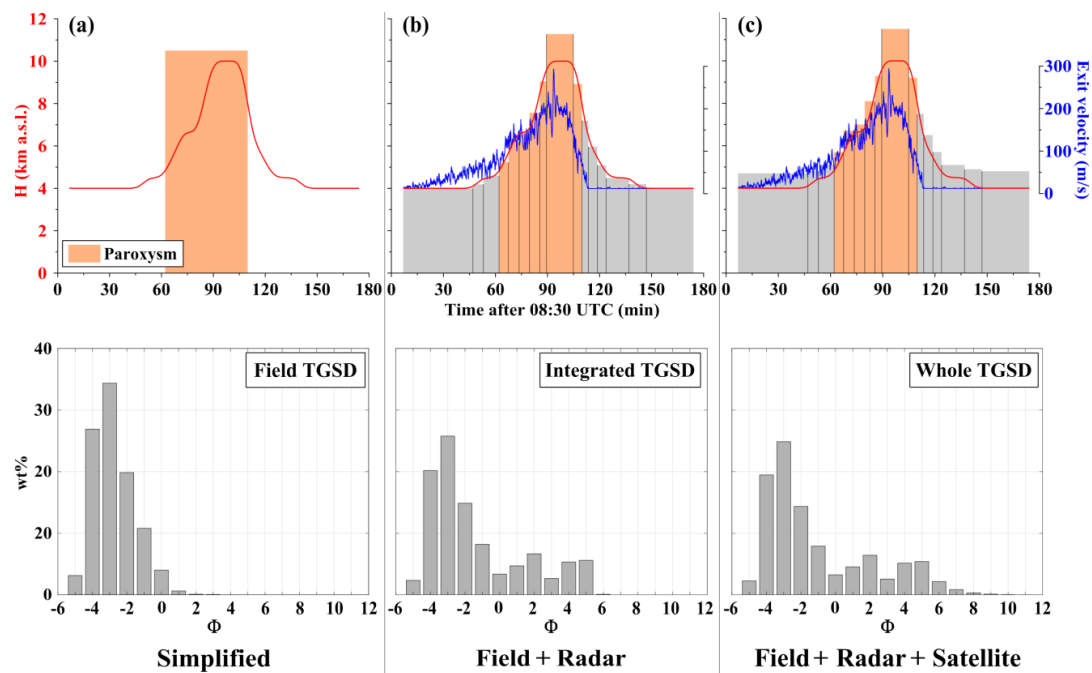
Figure 8: a) Comparative study between the measured and the computed tephra loadings for the Integrated TGSD. b) Graphic of the *k* index showing the optimization for assessing the best weights combination for both the Field and Radar TGSDs (details in Table 2)
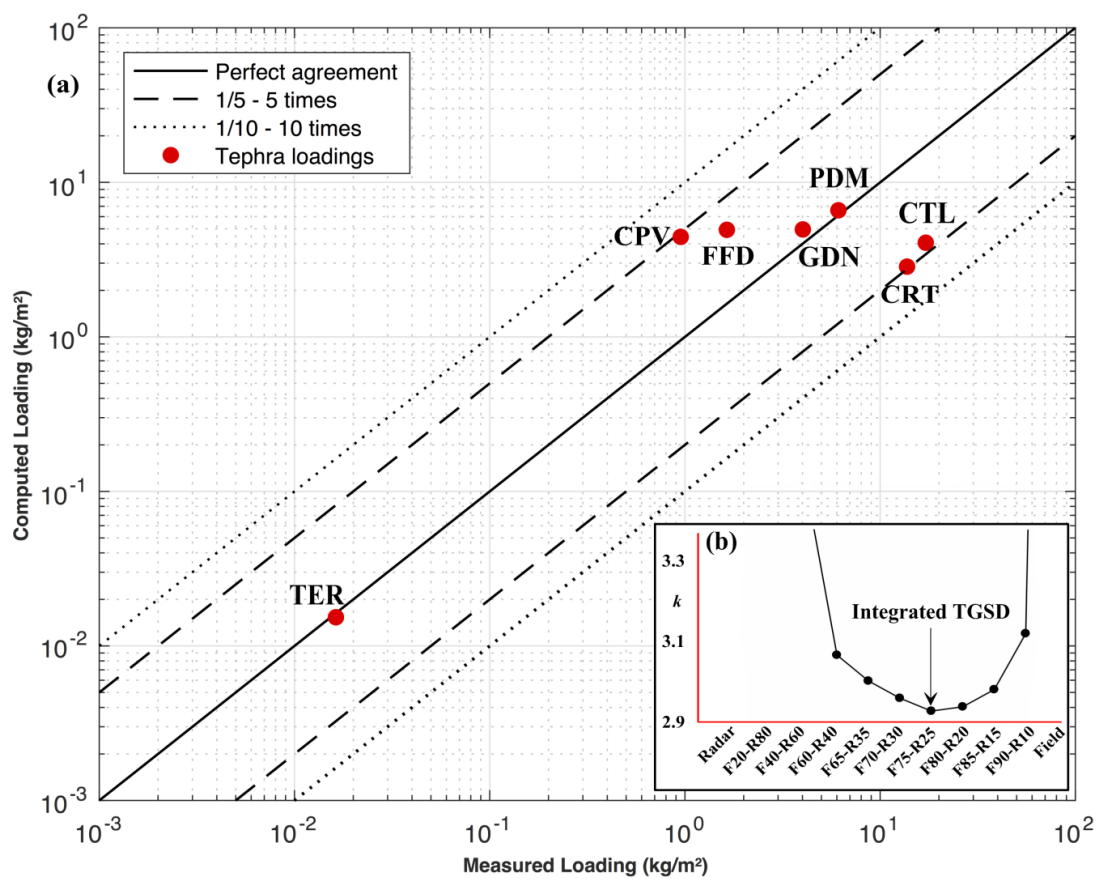
Atmospheric
Chemistry
and Physics
Discussions

Figure 9: Quantitative analysis of the airborne ash mass measured from SEVIRI and computed by FALL3D to assess the PM$_{20}$ fraction of the Whole TGSD necessary for best reproducing the far-travelling tephra. The upper part compares the whole airborne ash masses for the entire eruption, whereas the middle part gives the difference of the absolute average difference of mass per unit area. The lower part quantifies the difference in terms of mass per unit area.
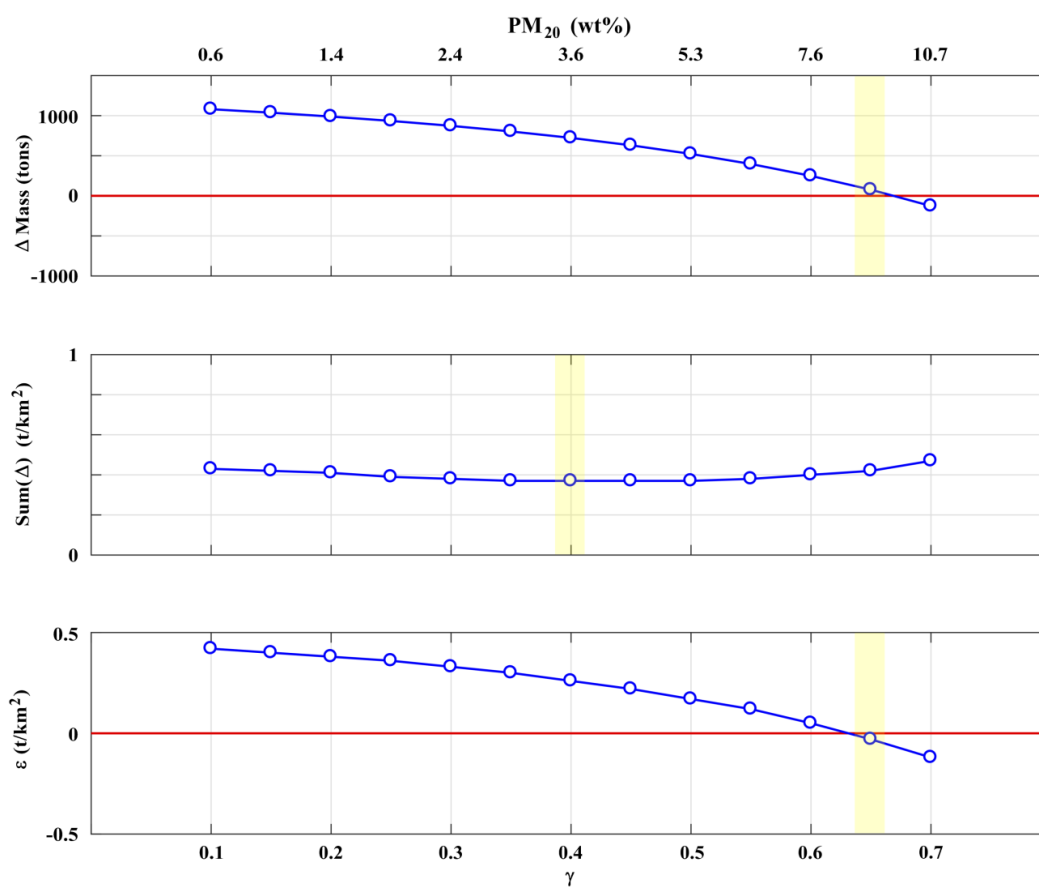
5

Figure 10: Tephra loading maps computed with the a) Field, b) Radar, c) Integrated and d) Whole TGSDs, respectively. They indicate the relevance of the integrated approach by validating the tephra fallout expansion and the affected areas.

Atmospheric
Chemistry
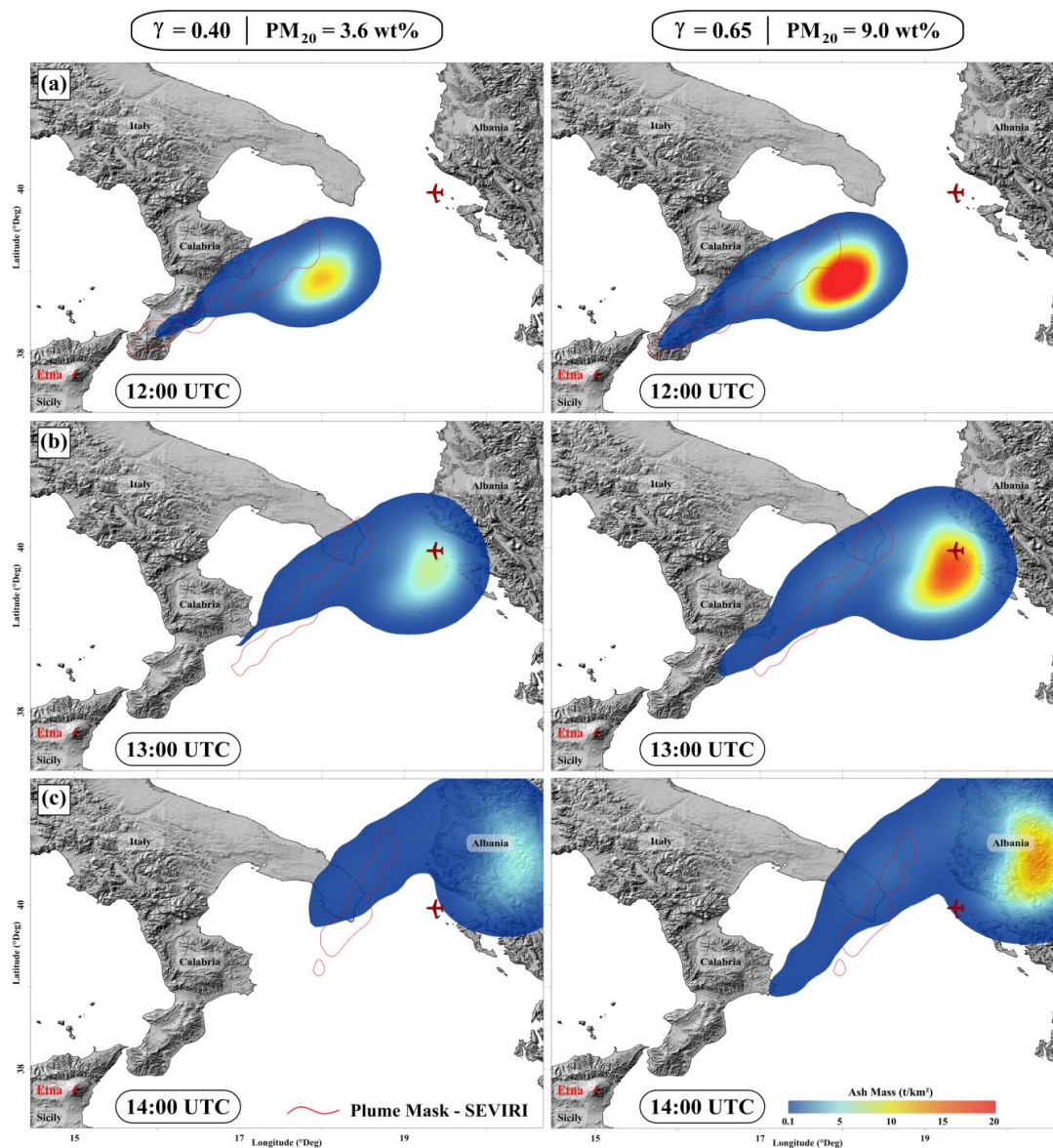and Physics
Discussions

Figure 11: Illustration of the comparative study between the SEVIRI and FALL3D airborne ash masses for a given time (i.e. 12:00, 13:00 and 14:00). The procedure aims at inverting the PM$_{20}$ fraction range to best reproduce the satellite retrievals (i.e. 3.6-9.0 wt%). The inversion implies the investigation of different γ factor values (associated with a PM$_{20}$ fraction) within the Whole TGSD.